Nanoscale Advances

ROYAL SOCIETY OF CHEMISTRY

PAPER

View Article Online
View Journal | View Issue

Cite this: *Nanoscale Adv.*, 2021, **3**, 550

Hydrothermal syntheses, luminescent properties, and temperature sensing of monodisperse Tb-doped $NaCeF_4$ nanocrystals†

Haoran Qin,[ab] Xinghong Gong,[a] Zundu Luo[a] and Yidong Huang *[a]

Received 10th September 2020
Accepted 27th November 2020

DOI: 10.1039/d0na00763c

rsc.li/nanoscale-advances

Monodisperse Tb-doped $NaCeF_4$ nanocrystals were synthesized *via* a hydrothermal method. The morphology, and room temperature and temperature dependent luminescent properties were investigated. Excited at 254 nm, the emissions of Ce^{3+} at 270–370 nm and those of Tb^{3+} at 475–700 nm can be observed. The strongest visible emission was observed in $NaCeF_4$:20 at% Tb with a quantum yield of 49%. The efficiency of energy transfer from Ce^{3+} to Tb^{3+} increases with the Tb^{3+} doping concentration and reaches 95% for $NaCeF_4$:30 at% Tb. The ratio of Tb^{3+} emission to Ce^{3+} emission is sensitive to temperature, and the relative sensitivity was calculated to be 1.0% $°C^{-1}$ at 60 °C. The mechanisms for this thermal dependence were analyzed in terms of non-radiative relaxation and energy migration.

Introduction

Lanthanide doped nano-fluorides have gained increasing attention due to their high chemical stability and high resistance to photobleaching.[1] Doped lanthanides give nanocrystals (NCs) unique f–f emission peaks and long fluorescence lifetimes.[2,3] These properties make lanthanide doped NCs appliable for biological labelling,[4] displays,[5,6] solar cells,[7] *etc.* A nano hexagonal β-$NaReF_4$ (Re = Y, La–Lu) system as a host for a luminescent temperature probe is mainly due to its good chemical and physical stability and highly efficient up-conversion and downshifting photoluminescence.[8,9]

Lanthanide ion Ce^{3+} possesses low 4f–5d multiplets and simple 4f multiplets and is widely applied for lanthanide luminescence.[10,11] Some monodisperse and well-defined $NaCeF_4$ based NCs have been synthesized. Lei *et al.* synthesized $NaCeF_4$:Er^{3+}/Yb^{3+} NCs *via* the high temperature coprecipitation method.[12] Li *et al.* synthesized $NaCeF_4$ NCs *via* the liquid–solid-solution hydrothermal method.[13]

Ce^{3+} ions possess broad absorption and emission bands with large cross-sections due to the high oscillator strength of parity allowed 4f–5d transition. The Tb^{3+} ion possesses green emission with a long fluorescence lifetime (millisecond scale), and has been applied for time-resolved photoluminescence imaging.[14] However, the absorption of excitation light by Tb^{3+} is weak because the corresponding 4f–4f transitions are all parity and spin forbidden. Efficient energy transfer (ET) from Ce^{3+} to Tb^{3+} and bright green emission have been reported in many Ce^{3+} & Tb^{3+} co-doped materials,[15–18] which inspired researchers to adopt Ce^{3+} and Tb^{3+} combination in nanomaterials. These materials can downshift ultra violet (UV) light to visible light to overcome the poor response of photovoltaic (PV) devices to short wavelength light.[19,20] Lian *et al.* synthesized $NaCeF_4$ and $NaCeF_4$:Tb^{3+} NCs *via* the thermal decomposition method,[21] and investigated their photoluminescence properties. The NCs synthesized *via* thermal decomposition are monodisperse and highly crystalline.[22] However the thermal decomposition method operates at high temperature (about 300 °C).[23] Here we synthesized $NaCeF_4$:Tb^{3+} NCs by a hydrothermal method.[24] With this method, the reaction operates at low temperature (below 200 °C) and monodisperse NCs were successfully synthesized.

Moreover, the 5d–4f emission of Ce^{3+} is sensitive to temperature,[25] while the 4f–4f emission of Tb^{3+} is not, which may be because the 4f multiplets are shielded by outer 5s and 5p multiplets.[26] With the different responses to temperature between Ce^{3+} and Tb^{3+}, their fluorescence intensity ratio (FIR) may act as a probe for temperature sensing. Some Ce^{3+} & Tb^{3+} co-doped phosphors have been investigated.[27–29] However, investigations on Ce^{3+} and Tb^{3+} induced FIR temperature sensing in NCs are rare.

In this article, we synthesized $NaCeF_4$:Tb^{3+} NCs by a hydrothermal method. The morphology and structure of $NaCeF_4$:Tb NCs were investigated. Furthermore, room temperature (RT) and temperature dependent luminescent properties of $NaCeF_4$:Tb NCs were studied. The materials are monodispersed and exhibit bright emission and a high quantum yield, and may

[a]*Key Laboratory of Optoelectronic Materials Chemistry and Physics, Fujian Institute of Research on the Structure of Matter, Chinese Academy of Sciences, Fuzhou, Fujian 350002, China. E-mail: huyd@fjirsm.ac.cn*

[b]*University of Chinese Academy of Sciences, Beijing 100039, China*

† Electronic supplementary information (ESI) available. See DOI: 10.1039/d0na00763c

have potential application for enhancing the energy conversion efficiency of PV devices. Moreover, since the FIR between Ce^{3+} and Tb^{3+} emission correlates strongly with temperature, $NaCeF_4$:Tb NCs may have potential application in FIR nanothermometers.

Experimental

Materials

$Ce(NO_3)_3 \cdot 6H_2O$, $Tb(NO_3)_3 \cdot 5H_2O$, oleic acid (OA), sodium hydroxide, ammonium fluoride, and cyclohexane were purchased from the Aladdin Chemical Reagent Company. Ethanol was purchased from the Sinopharm Chemical Reagent Company. All the chemicals were of analytical grade and used without further purification. Deionized water was used throughout the experiments.

Synthesis

Typically, for synthesis of $NaCeF_4$ NCs, 1.5 ml H_2O, 0.6 g sodium hydroxide, 20 ml OA, and 10 ml ethanol were mixed. Then 0.5 mmol $Ce(NO_3)_3$ (0.5 M) aqueous solution was added into the above solution. Lastly, 3 mmol ammonium fluoride aqueous solution (2 M) was added into the mixed solution. After stirring for 30 min, the colloidal solution was transferred into a 50 ml Teflon-lined autoclave and was heated at selected 170 °C for 6 h. The systems were then cooled down to room temperature. The final products were collected by centrifugation, washed with ethanol, and then dispersed in cyclohexane. The doping of Tb^{3+} was conducted by adding $Tb(NO_3)_3$ with designed concentrations to the reaction system.

Characterization

X-ray diffraction (XRD) analysis was carried out on a Rigaku-Dmax 2500 diffractometer using Cu-Kα radiation ($\lambda = 0.154$ nm). The size and morphology of the samples were observed using a transmission electron microscope (TEM) JEOL-2010 equipped with an energy dispersive X-ray spectrometer (EDS). Fourier-transform infrared (FTIR) spectra were recorded in KBr discs using a Magna 750 FTIR spectrometer. The temperature dependent and RT emission, RT excitation spectra, quantum yield, and RT fluorescence decay curves were recorded from pressed tablets of the $NaCeF_4$:Tb NCs powder using an FLS 980, Edinburgh.

Results and discussion

Components and morphology

The XRD patterns of $NaCeF_4$ NCs with different Tb^{3+} doping concentrations match well with those of β-$NaCeF_4$ (pdf#50-0154) (ESI Fig. S1†). No additional phases were found even in the sample with 30 at% Tb^{3+} doping, indicating that Tb^{3+} has been efficiently incorporated into the host of β-$NaCeF_4$. The EDS pattern of $NaCeF_4$:20 at% Tb is shown in ESI Fig. S2.† The results of XRD and EDS analyses reveal high purity of the as-prepared samples. OA was chosen as the capping agent to control the growth of NCs and make NCs non-polar solvent soluble. The as-prepared NCs can be well dispersed in cyclohexane and the solution is transparent (ESI Fig. S3(a)†). The presence of OA capping on the surface of the $NaCeF_4$ NCs was verified from the FTIR spectrum (ESI Fig. S3(b)†).

The TEM pattern of $NaCeF_4$:20 at% Tb NCs is shown in Fig. 1. The shape and size of the asprepared NCs can be seen in Fig. 1(a–c); the NCs are a hexagonal prism and monodisperse. The length of NCs is parallel to the hexad axis, and hence the crystal growth direction is [001]. The length of $NaCeF_4$:20 at% Tb NCs has been estimated by randomly analysing 200 NCs. The mean length of the NCs is 170 nm and the distribution frequency of the lengths can be seen in Fig. 1(d), which shows good uniformity of the NCs. The cross-section diameters of the NCs are about 45 nm. The aspect ratio of the NCs was therefore calculated to be 3.8. From the high resolution TEM (HRTEM) image of the NC pattern shown in Fig. 1(e), clear lattice fringes can be observed, which indicate good crystallinity. Fig. 1(f) shows the Fourier transform image of the square area in

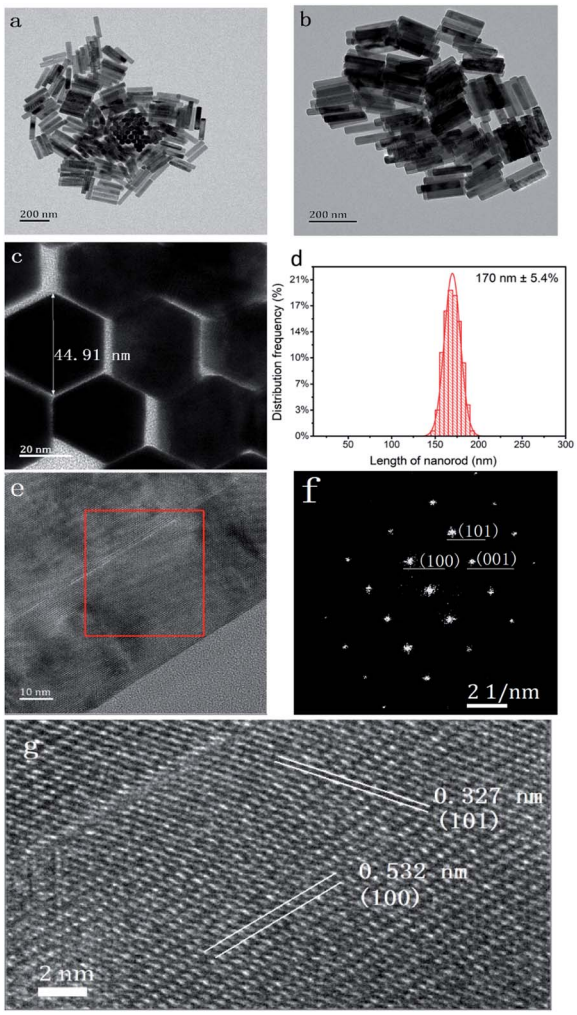

Fig. 1 (a and b) TEM images of $NaCeF_4$:20 at% Tb NCs. (c) HRTEM image of the NCs. (d) Distribution frequency of the lengths of the NCs. (e) HRTEM image of the NCs. (f) Fourier transform image of the square area in (e). (g) Zoom in of the square area in (e) with the labelled interplanar spacing.

Fig. 1(e). In Fig. 1(g), two interplanar distances were labelled 0.532 and 0.327 nm, which are in accordance with the (100) and (101) interplanar distances of $NaCeF_4$,[30] respectively.

Luminescent properties

The excitation spectra of the $NaCeF_4$:Tb NCs are similar, and the excitation spectrum of the $NaCeF_4$:20 at% Tb monitoring emission at 543 nm is shown in Fig. 2. There are two types of excitation signals in Fig. 2. The broad and strong band originates mainly from the parity-allowed 4f–5d transitions of Ce^{3+}, and the narrow and weak peaks come from the parity-forbidden 4f–4f transitions from the ground state to the corresponding excited multiplets of Tb^{3+}. The strong band is centered at 256 nm and matches well with a commercial low-pressure mercury lamp with a central wavelength of 254 nm. Under excitation of the lamp, the cyclohexane solution with $NaCeF_4$:20 at% Tb NCs dispersed emits bright green fluorescence (ESI Fig. S4†). Under excitation at 254 nm, the emission spectra of the $NaCeF_4$ NCs with different Tb doping concentrations are shown in Fig. 3(a). The emission spectra for different samples were measured under the same conditions. The broad emission bands around 305 nm originate from the 5d–4f transition of Ce^{3+}. The emission peaks centered at 489, 543, 584, and 620 nm are the 4f–4f transitions from $^5D_4$ to $^7F_{6,5,4,3}$ multiplets of Tb^{3+}, respectively. Fig. 3(b) shows the changes of fluorescence intensities at 305 and 543 nm with the Tb doping concentration. Fluorescence intensity at 305 nm decreases with the increase of the Tb concentration, which indicates the existence of the ET process from Ce^{3+} to Tb^{3+}. The Ce^{3+} emission ranges from 275 to 360 nm, which overlaps with some excited levels of Tb^{3+} (ESI Fig. S5†). Hence the ET from Ce^{3+} to Tb^{3+} is resonant. The ET efficiency can be expressed by the following equation:[31]

$$\eta_T = 1 - \frac{I_S}{I_{S0}}$$

where I_S and I_{S0} are the integrated fluorescence intensities (270–370 nm) of Ce^{3+} with and without Tb^{3+} doping, respectively. The ET efficiency for the $NaCeF_4$:$x$at% Tb NCs (x = 1, 3, 5, 10, 15, 20, 25, 30) was therefore calculated to be 10%, 16%, 45%, 63%, 71%, 78%, 88%, and 95%, respectively. In Fig. 3, the sample with 20 at% Tb doping shows the strongest visible emission and the visible quantum yield was measured to be 49%. With the Tb doping concentration being increased further, the intensity of Tb emission decreases, which indicates the presence of concentration dependent fluorescence quenching in the NCs.

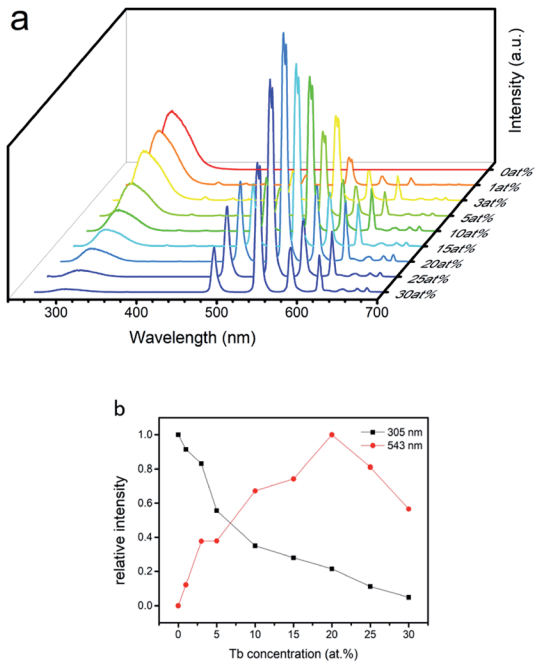

Fig. 3 (a) Emission spectra of $NaCeF_4$:Tb NCs under excitation at 254 nm. (b) Fluorescence intensity at 305 and 543 nm *versus* the Tb concentration.

Fluorescence decay curves at 543 nm for $NaCeF_4$ NCs with different Tb doping concentrations were measured under excitation at 254 nm. The results on a semilog coordinate are depicted in Fig. 4. Obviously, the curves exhibit simple exponential decay behaviour and can be expressed by

$$I = I_0 \exp(-t/\tau)$$

where I is the fluorescence intensity at time t, I_0 is the fluorescence intensity at $t = 0$, and τ is the fluorescence lifetime of the excited multiplet $^5D_4$. With the Tb concentration being increased from 1 at% to 30 at%, the fluorescence lifetime

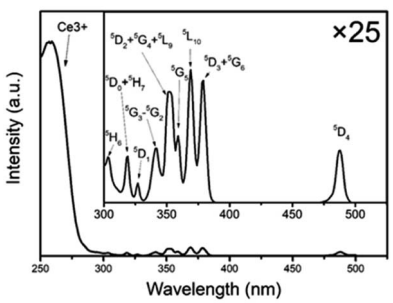

Fig. 2 Excitation spectrum of $NaCeF_4$:20 at% Tb NCs monitoring at Tb^{3+} $^5D_4 \rightarrow {}^7F_5$ transition (λ_{em} = 543 nm). The inset spectrum is intensity magnified 25 times the one in the range from 300 to 550 nm.

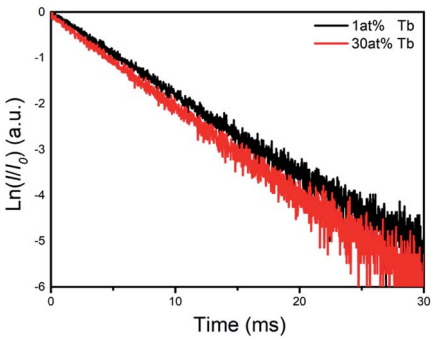

Fig. 4 Semi-logarithmic coordinates of the fluorescence decay curves of Tb^{3+} $^5D_4 \rightarrow {}^7F_5$ transition (λ_{em} = 543 nm) under excitation at 254 nm for the sample with different Tb doping concentrations.

decreases from 5.59 to 4.97 ms. The fluorescence lifetime maintains at the millisecond level for high Tb doping concentrations.

Temperature sensing behaviour

$NaCeF_4$:5 at% Tb NCs exhibit high and similar Ce and Tb emission intensities, which are suitable for temperature sensing.[32] The temperature dependent fluorescence spectra of $NaCeF_4$:5 at% Tb NCs under excitation at 254 nm are shown in Fig. 5(a). The trends of the temperature dependent emission intensity of Ce^{3+} and Tb^{3+} are different. I_{Ce} is defined as the integrated Ce^{3+} emission intensity in the range of 270–370 nm. I_{Tb} and $I_{Tb\ green}$ are defined as the integrated Tb^{3+} emission intensities in the ranges of 475–700 nm and 525–570 nm, respectively. As shown in Fig. 5(b), when the temperature is below 0 °C, I_{Ce} remains unchanged (100% ± 2%); when the temperature is higher than 0 °C, I_{Ce} decreases with temperature rise and to 83% at 60 °C. However, bot I_{Tb} and $I_{Tb\ green}$ increase with the temperature to about 150% at 60 °C. Based on the Ce^{3+} configuration coordinate diagram shown in Fig. 6, the trend of temperature dependent I_{Ce} can be partially explained. The nonradiative transition (process A) needs assistance of phonons to pass through an energy barrier ΔE to the 4f ground states,[33] and hence increasing the temperature will promote this nonradiative transition[34] and decrease the overall quantum efficiency. The temperature dependent luminescence spectra of $NaCeF_4$ NCs can be seen in ESI Fig. S6.† ΔE was calculated to be 0.41 eV according to the Arrhenius formula. For materials with a high Ce^{3+} concentration, there is another temperature quenching mechanism: thermally activated concentration quenching.[35] This mechanism depends on the thermally enhanced nonradiative energy migration among Ce^{3+} and then transfer to defects.[36] For Tb^{3+} and Ce^{3+} co-doped materials, the defects could also be Tb^{3+}. Hence, Tb^{3+} emission could be thermally enhanced in materials with a high Ce^{3+} concentration. $NaCeF_4$:Tb^{3+} possesses a high Ce^{3+} concentration, and hence temperature sensitivity may be higher than those with a low Ce^{3+} concentration.

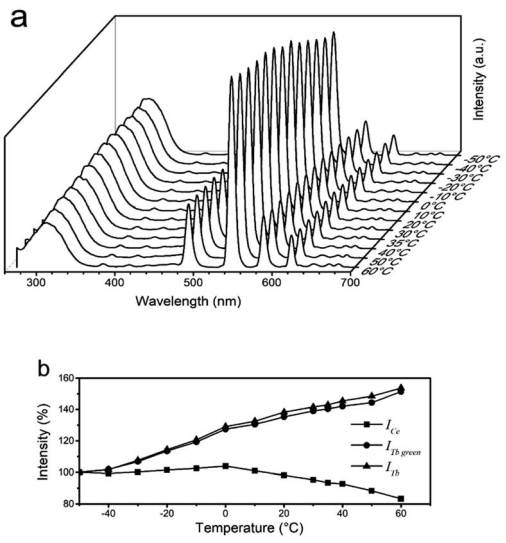

Fig. 5 (a) Temperature dependent luminescence spectra of $NaCeF_4$:5 at% Tb NCs. (b) Integrated luminescence intensity *versus* temperature.

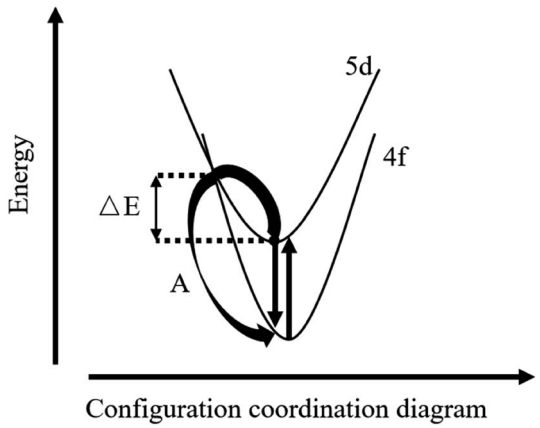

Fig. 6 Ce^{3+} configuration coordinate diagram.

As illustrated in Fig. 7(a and b), both the FIRs I_{Tb}/I_{Ce} and $I_{Tb\ green}/I_{Ce}$ increased monotonously and nonlinearly with temperature. The experimental values in Fig. 7(a and b) can be fitted well with single exponential curves; the relevant expressions are

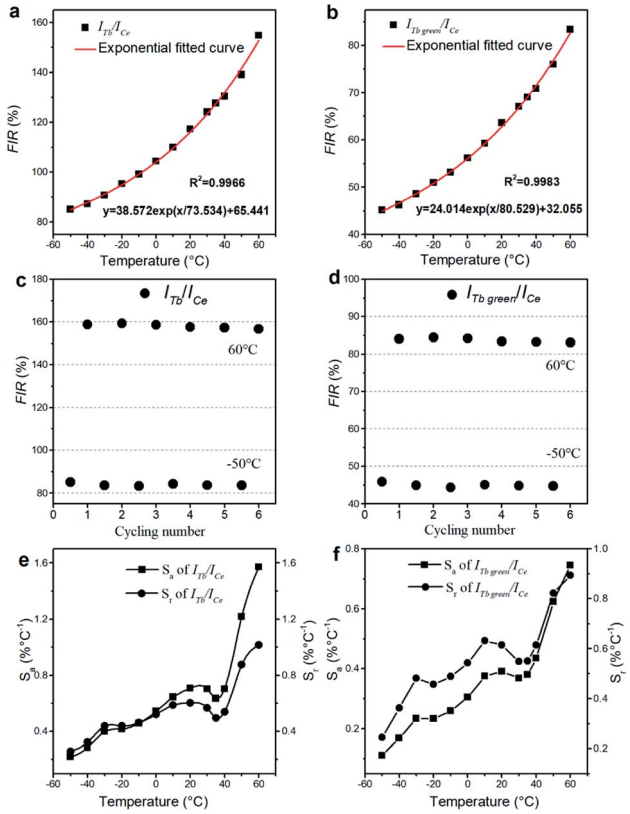

Fig. 7 For $NaCeF_4$:5 at% Tb NCs. (a and b) Temperature dependent fluorescence intensity ratio with exponential fitted curves (I_{Tb}/I_{Ce} for (a); $I_{Tb\ green}/I_{Ce}$ for (b)). (c and d) I_{Tb}/I_{Ce} and $I_{Tb\ green}/I_{Ce}$ in heating–cooling cycles. (e and f) Temperature dependent absolute sensitivity (S_a) and relative sensitivity (S_r) (I_{Tb}/I_{Ce} for (e); $I_{Tb\ green}/I_{Ce}$ for (f)).

Table 1 Summary of the Ce^{3+} concentration, tendency of the I_{Ce}/I_{Tb} ratio with temperature, temperature range and Sr of $NaCeF_4$:5% Tb and some Ce & Tb thermometers

Ce & Tb activated thermometers	Ce^{3+} concentration (10^{20} cm^{-3})	Tendency of the I_{Ce}/I_{Tb} ratio with temperature	Temperature range (°C)	Sr (% $°C^{-1}$)	Ref.
YBO_3:1% Ce,1% Tb	1.8	Linear	15–55	0.498	37
β-$NaYF_4$:10% Ce,5% Tb	12.2	Linear	30–290	0.65	38
LaOBr: 1% Ce,3% Tb	1.6	Linear	20–160	0.42	27
$K_2BaCa(PO_4)_2$:3% Ce,3% Tb	3.0	Linear	20–200	0.35	39
$Sr_{30.6}Ce(PO_4)_3$:40% Tb	22.7	Linear	25–300	0.384	40
$BaY_2Si_3O_{10}$:2% Ce,18% Tb	1.9	Linear	20–260	0.30	41
$NaCeF_4$:5% Tb	112.6	Nonlinear	−50 to 60	1.0	This work

shown as insets in Fig. 7(a and b), respectively. Repeatability and stability are important for practical application of thermometers. Six cycles of heating–cooling experiments were thus conducted, and the results are shown in Fig. 7(c and d). The results indicate that I_{Tb}/I_{Ce} and $I_{Tb\ green}/I_{Ce}$ are reversible and stable. The absolute and relative sensitivity (S_a, S_r) can be expressed as[42]

$$S_a = \left|\frac{dFIR}{dT}\right|$$

$$S_r = \left|\frac{1}{FIR} \times \frac{dFIR}{dT}\right|$$

where T is the temperature. The calculated S_a and S_r *versus* temperature were plotted in Fig. 7(e and f). The values of S_r for I_{Tb}/I_{Ce} and $I_{Tb\ green}/I_{Ce}$ below 40 °C are similar. When the temperature exceeds 40 °C, the S_r of I_{Tb}/I_{Ce} is larger than that of $I_{Tb\ green}/I_{Ce}$. The maximum S_r of I_{Tb}/I_{Ce} and $I_{Tb\ green}/I_{Ce}$ reaches 1.0% $°C^{-1}$ and 0.9% $°C^{-1}$ at 60 °C, respectively, and the values may be higher at a higher temperature. In Table 1, compared with others, the tendency of the I_{Ce}/I_{Tb} ratio with temperature for $NaCeF_4$:5% Tb is unique and $NaCeF_4$:5% Tb has the highest Sr, which may be ascribed to its highest Ce^{3+} concentration. The high temperature sensitivity and high stability indicate that this NC could be a candidate for use as a UV-excited luminescence ratio metric nanothermometer.

Conclusion

Monodisperse Tb doped $NaCeF_4$ NCs with high crystallinity and high uniformity have been prepared *via* a hydrothermal method. Under excitation at 254 nm, the NCs exhibit UV emission of Ce^{3+} and characteristic visible emission of Tb^{3+}. Fluorescence spectra show the existence of ET from Ce^{3+} to Tb^{3+}, and $NaCeF_4$:20 at% Tb displays the strongest visible emission with a quantum yield of 49%. The temperature dependent fluorescence spectra of $NaCeF_4$:5 at% Tb indicate that the ratio of Tb emission to Ce emission increases monotonously with temperature. Compared with other Ce & Tb thermometers, the Tb doped $NaCeF_4$ NCs have higher maximum S_r, which may be ascribed to the high Ce^{3+} concentration in the NCs. Due to the uniform nanomorphology, unique luminescent properties and high temperature sensitivity, the Tb doped $NaCeF_4$ NCs may have applications in PV devices and FIR nanothermometers.

Conflicts of interest

There are no conflicts to declare.

Acknowledgements

This work has been supported by the National Natural Science Foundation of China (Grant 51772290).

References

1 T. Cheng, R. Marin, A. Skripka and F. Vetrone, *J. Am. Chem. Soc.*, 2018, **140**, 12890–12899.
2 J. Liu, A. M. Kaczmarek and R. Van Deun, *Chem. Soc. Rev.*, 2018, **47**, 7225–7238.
3 K. Y. Zhang, Q. Yu, H. Wei, S. Liu, Q. Zhao and W. Huang, *Chem. Rev.*, 2018, **118**, 1770–1839.
4 Q. Ma, J. Wang, Z. Li, X. Lv, L. Liang and Q. Yuan, *Small*, 2019, **15**, 1804969.
5 F. Wang, Y. Han, C. S. Lim, Y. Lu, J. Wang, J. Xu, H. Chen, C. Zhang, M. Hong and X. Liu, *Nature*, 2010, **463**, 1061–1065.
6 W. Song, H. Choi, Y. Kim and H. Yang, *J. Mater. Chem.*, 2010, **20**, 6929–6934.
7 J. Roh, H. Yu and J. Jang, *ACS Appl. Mater. Interfaces*, 2016, **8**, 19847–19852.
8 W. You, D. Tu, W. Zheng, X. Shang, X. Song, S. Zhou, Y. Liu, R. Li and X. Chen, *Nanoscale*, 2018, **10**, 11477–11484.
9 D. Peng, Q. Ju, X. Chen, R. Ma, B. Chen, G. Bai, J. Hao, X. Qiao, X. Fan and F. Wang, *Chem. Mater.*, 2015, **27**, 3115–3120.
10 Q. Yao, P. Hu, P. Sun, M. Liu, R. Dong, K. Chao, Y. Liu, J. Jiang and H. Jiang, *Adv. Mater.*, 2020, **32**, 1907888.
11 B. Zhou, J. Huang, L. Yan, X. Liu, N. Song, L. Tao and Q. Zhang, *Adv. Mater.*, 2019, **31**, 1806308.
12 X. Lei, R. Li, D. Tu, X. Shang, Y. Liu, W. You, C. Sun, F. Zhang and X. Chen, *Chem. Sci.*, 2018, **9**, 4682–4688.
13 S. Li, T. Xie, Q. Peng and Y. Li, *Chem.–Eur. J.*, 2009, **15**, 2512–2517.
14 D. Tu, L. Liu, Q. Ju, Y. Liu, H. Zhu, R. Li and X. Chen, *Angew. Chem., Int. Ed.*, 2011, **50**, 6306–6310.

15 X. Wu, Y. Jiao, O. Hai, Q. Ren, F. Lin and H. Li, *J. Alloys Compd.*, 2018, **730**, 521–527.
16 J. Huo, L. Dong, W. Lu, B. Shao and H. You, *Phys. Chem. Chem. Phys.*, 2017, **19**, 17314–17323.
17 A. Yanes, J. del-Castillo and E. Ortiz, *J. Alloys Compd.*, 2019, **773**, 1099–1107.
18 L. Sun, B. Devakumar, J. Liang, S. Wang, Q. Sun and X. Huang, *J. Mater. Chem. C*, 2019, **7**, 10471–10480.
19 D. Yim, I. Cho, S. Lee, C. Kwak, D. Kim, J. Lee and K. Hong, *J. Nanosci. Nanotechnol.*, 2011, **11**, 8748–8753.
20 J. Velázquez, V. Rodríguez, A. Yanes, J. Del-Castillo and J. Méndez-Ramos, *Opt. Mater.*, 2012, **34**, 1994–1997.
21 H. Lian, Y. Dai, D. Yang, Z. Cheng, C. Li, Z. Hou, M. Shang and J. Lin, *Nanoscale*, 2014, **6**, 9703–9712.
22 J. Boyer, F. Vetrone, L. Cuccia and J. Capobianco, *J. Am. Chem. Soc.*, 2006, **128**, 7444–7445.
23 S. Gai, C. Li, P. Yang and J. Lin, *Chem. Rev.*, 2014, **114**, 2343–2389.
24 X. Wang, J. Zhuang, Q. Peng and Y. Li, *Nature*, 2005, **437**, 121–124.
25 M. Weber, *Solid State Commun.*, 1973, **12**, 741–744.
26 Y. Lin, M. Bettinelli and M. Karlsson, *Chem. Mater.*, 2019, **31**, 3851–3862.
27 X. Zhang, Y. Huang and M. Gong, *Chem. Eng. J.*, 2017, **307**, 291–299.
28 M. Ding, C. Lu, L. Chen and Z. Ji, *J. Alloys Compd.*, 2018, **763**, 85–93.
29 W. Dai, J. Hu, G. Liu, S. Xu, K. Huang, J. Zhou and M. Xu, *J. Lumin.*, 2020, **217**, 116807.
30 A. Grzechnik and K. Friese, *Dalton Trans.*, 2012, **41**, 10258–10266.
31 P. Paulose, G. Jose, V. Thomas, N. Unnikrishnan and M. Warrier, *J. Phys. Chem. Solids*, 2003, **64**, 841–846.
32 C. D. Brites, S. Balabhadra and L. D. Carlos, *Adv. Opt. Mater.*, 2019, **7**, 1801239.
33 C. Struck and W. Fonger, *J. Lumin.*, 1975, **10**, 1–30.
34 C. R. Ronda, *Luminescence: from theory to applications*, John Wiley & Sons, 2007.
35 W. Yen, S. Shionoya and H. Yamamoto, *Phosphor Handbook*, CRC Press, Boca Raton, 2006.
36 D. Dexter and J. Schulman, *J. Chem. Phys.*, 1954, **22**, 1063–1070.
37 M. Li, F. You, C. Liang and Z. He, *J. Alloys Compd.*, 2020, **833**, 155011.
38 M. Ding, C. Lu, L. Chen and Z. Ji, *J. Alloys Compd.*, 2018, **763**, 85–93.
39 F. Mo, X. Zhang, Z. Sun, Z. Zhu, Z. Guo and Z. Wu, *Ceram. Int.*, 2019, **45**, 12319–12324.
40 W. Liu, X. Wang, Q. Zhu and J. G. Li, *J. Alloys Compd.*, 2020, **829**, 154563.
41 F. Qian and J. Zhang, *Mater. Res. Bull.*, 2020, **122**, 110660.
42 D. Jaque and F. Vetrone, *Nanoscale*, 2012, **4**, 4301–4326.